Electronic Supplementary Material (ESI) for Journal of Materials Chemistry C.

Supporting Information for

Tuning Charge Carrier Dynamics through Spacer Cation Functionalization in Layered Halide Perovskites: An ab initio Quantum Dynamics Study

Pabitra Kumar Nayak[1] and Dibyajyoti Ghosh[1,2]

[1]*Department of Chemistry, Indian Institute of Technology, Delhi, Hauz Khas, New Delhi-110016, India*

[2] *Department of Materials Science and Engineering (DMSE), Indian Institute of Technology, Delhi, Hauz Khas, New Delhi-110016, India*

Table S1. Optimized structural parameters for $(PhDMA)PbI_4$ and $(4F\text{-}PhDMA)PbI_4$.

Structural Parameters	**$(PhDMA)PbI_4$**	**$(4F\text{-}PhDMA)PbI_4$**
Interlayer distance (Å) (Closest I···I distance)	6.64	6.48
H_{NH3} and I of Pb-I-Pb distance (Å)	2.60	2.57
H_{NH3} and terminal I distance (Å)	2.46	2.40
Intra-spacer ortho H/F and methylene H distance (Å)	2.46	2.48
Inter-spacer ortho H/F and methylene H distance (Å)	2.58	2.37
Ortho H/F and terminal I distance (Å)	3.48	3.44
Intra-spacer ortho H/F and H of NH_3 distance (Å)	2.91	2.89
Inter-spacer ortho H/F and H of NH_3 distance (Å)	4.16	3.92
Equatorial tilt(α) angle (°)	18.8	18.9
Axial tilt(β) angle (°)	12.5	12.3
Equatorial Pb-I-Pb angle (°)	142.3	142.2
Equatorial Pb-I bond length (Å)	3.10	3.06
Axial Pb-I bond length (Å)	3.24	3.20
Equatorial dihedral angle (°)	19.8	21.2
Axial dihedral angle (°)	11.9	11.9

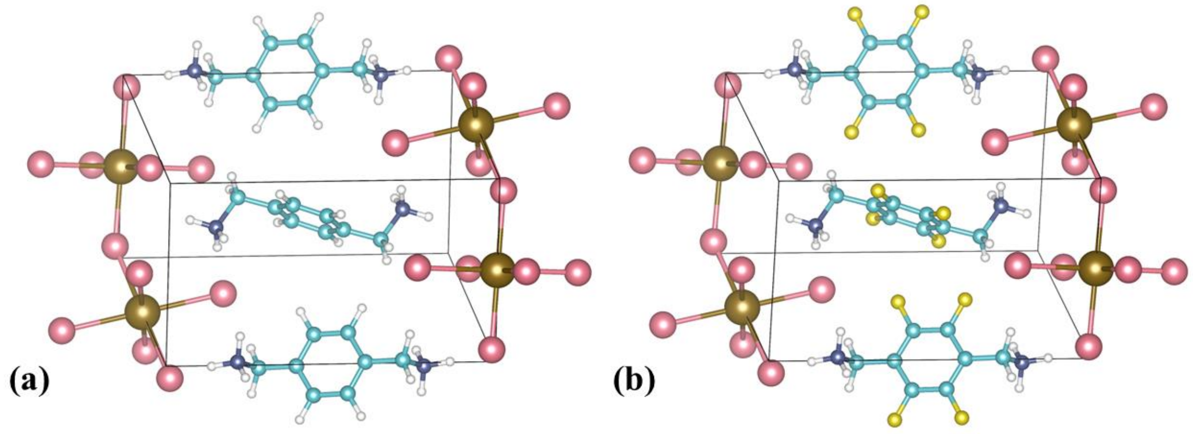

Figure S1. Optimized structure and spacer cation packing in the organic layer for (a) (PhDMA)PbI_4 and (b) (4F-PhDMA)PbI_4.

Section S1. Details of non-covalent index (NCI) calculations

In the NCI plot, the electron density (ρ) and its spatial reduced gradients $s(\vec{r})$ are used to understand the interaction between inorganic and organic sublattices of LHPs. In typical representation, the $s(\vec{r})$ are analyzed as a function of $\mathrm{sign}(\lambda_2)\rho$, where λ_2 is the second eigenvalue of the density (ρ) Hessian (second derivative) matrix. The troughs and singularities in plotted $s(\vec{r})$ represent the existence of non-covalent interactions in the system. Since the non-covalent interaction can be favorable or unfavorable, the sign of λ_2 is a key point to note. Overall, there are three regions in $s(\vec{r})$ vs. $\mathrm{sign}(\lambda_2)\rho$ plot, the trough (1) at zero (green, $\lambda_2 \sim 0$) are van der Waal interactions, (2) at the left (blue, $\lambda_2 < 0$) indicates attractive interactions, and (3) at the right (red, $\lambda_2 > 0$) are repulsive or unfavorable interactions.

In Figure 2 c-d, a pair of strong hydrogen bonds (deep blue lobes) form with axial iodide atoms, whereas relatively weaker bonds (pale blue) form with equatorial I.

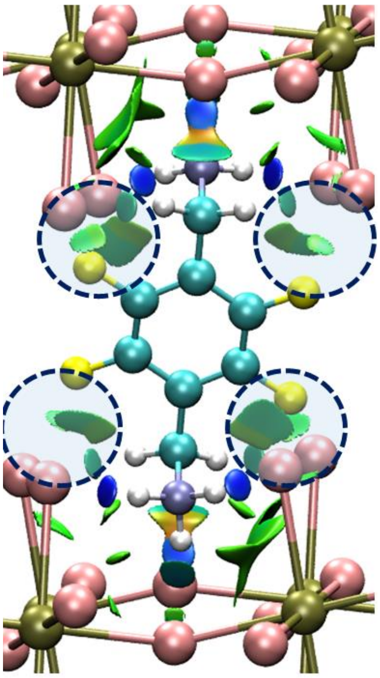

Figure S2. The zoomed NCI contour plot for (4F-PhDMA)PbI_4. The semitransparent blue circles point out the non-covalent F···I halogen interactions. A detailed discussion of these interactions is included in the Results and Discussion section of the main text.

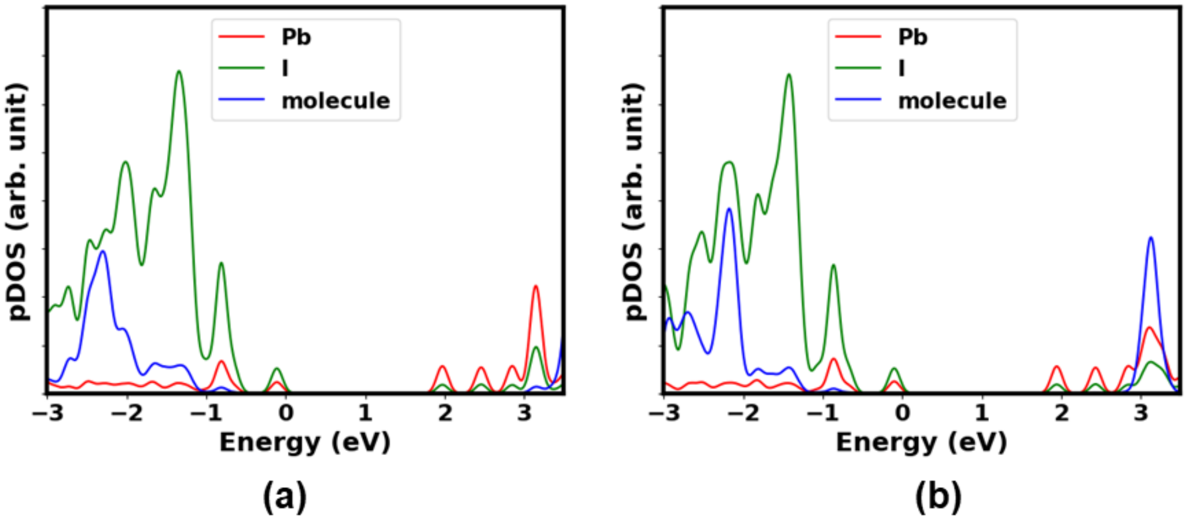

Figure S3. The partial density of states for optimized geometry of (a) (PhDMA)PbI_4 and (b) (4F-PhDMA)PbI_4. The VBM and CBM states are very similar for both materials, depicting the negligible impact of spacer cations on these energy states. The calculations consider hybrid HSE06 functionals and include spin-orbit coupling corrections.

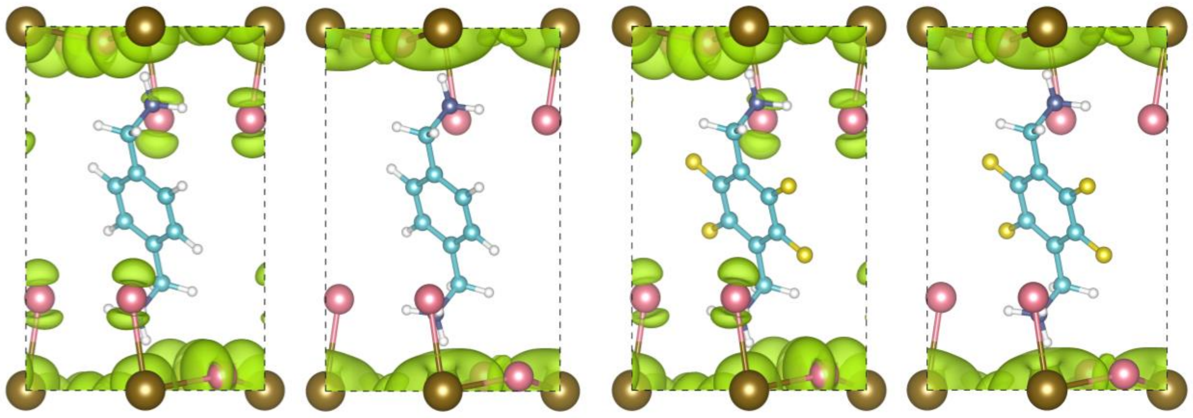

(a) (b) (c) (d)

Figure S4. The charge density of (a) VBM & (b) CBM for (PhDMA)PbI$_4$, and (c) VBM & (d) CBM for (4F-PhDMA)PbI$_4$.

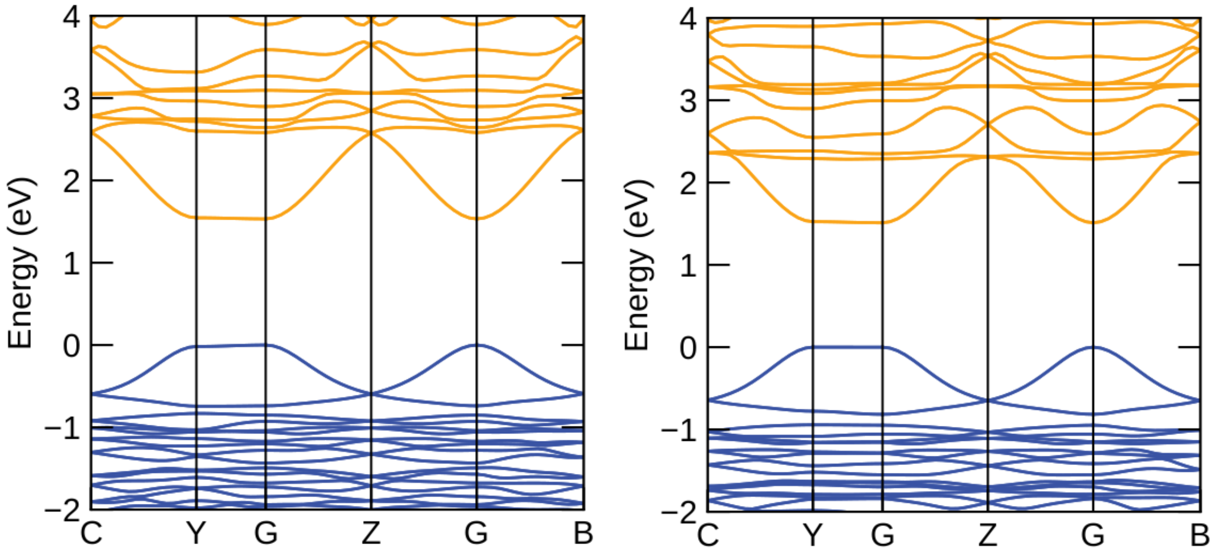

(a) (b)

Figure S5. The electronic band structure for (a) (PhDMA)PbI$_4$ and (b) (4F-PhDMA)PbI$_4$. Both LHPs are direct gap semiconductors where the band gap is located at the G(Γ)-point in the Brillouin zone. The calculations consider semilocal PBE-GGA functionals and include spin-orbit coupling corrections. We do not consider hybrid functional for band structure calculations as it does not impact the band structure significantly. The high-symmetry points are C (0.5, 0.5, 0), Y (0.5, 0.0, 0.0), G (0.0, 0.0, 0.0), Z (0.0, 0.5, 0.0), and B (0.0, 0.0, 0.5). Note that, the PbI-layers are stacked along G(Γ)→ Y direction. The band edges indicate strong dispersion of the VBM and CBM only along the inorganic plane (in-plane).

Table S2. Band gap and effective masses in different directions of (PhDMA)PbI$_4$ and (4F-PhDMA)PbI$_4$. Static band gaps and effective masses are calculated using optimized geometry at 0 K. Key: m_e is the free electron rest mass.

	Static HSE-SOC Band Gap (eV)	Static PBE bandgap (eV)	Time averaged PBE bandgap (eV)	Hole Effective Mass (m_e)	Electron Effective Mass (m_e)
(PhDMA)PbI$_4$	1.53	2.29	2.28	-0.30 (Γ→ Z) -0.31 (Γ→ B) -5.36 (Γ→ Y)	0.24 (Γ→ Z) 0.25 (Γ→ B) 7.31 (Γ→ Y)
(4F-PhDMA)PbI$_4$	1.51	2.22	2.21	-0.28 (Y→ C) -104.4 (Γ→ Y)	0.24 (Γ→ Z) 0.24 (Γ→ B) 8.16 (Γ→ Y)

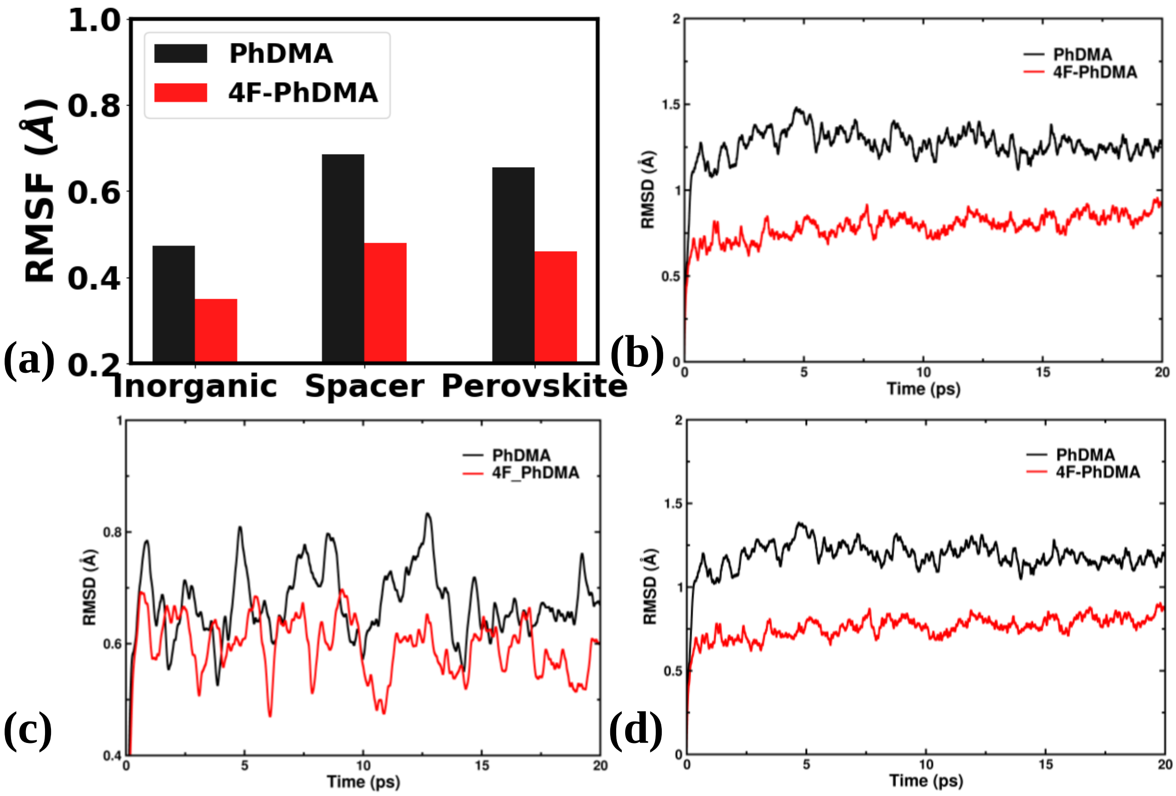

Figure S6. (a) The bar chart of root mean square fluctuation value for inorganic perovskite layer, organic spacer, and whole layered halide perovskite for both the perovskite materials. The root mean square deviation (RMSD) plot for (b) individual organic spacers, (c) inorganic perovskite framework, and (d) whole 2D-perovskites have been compared for both perovskites over all the trajectories of 20 ps.

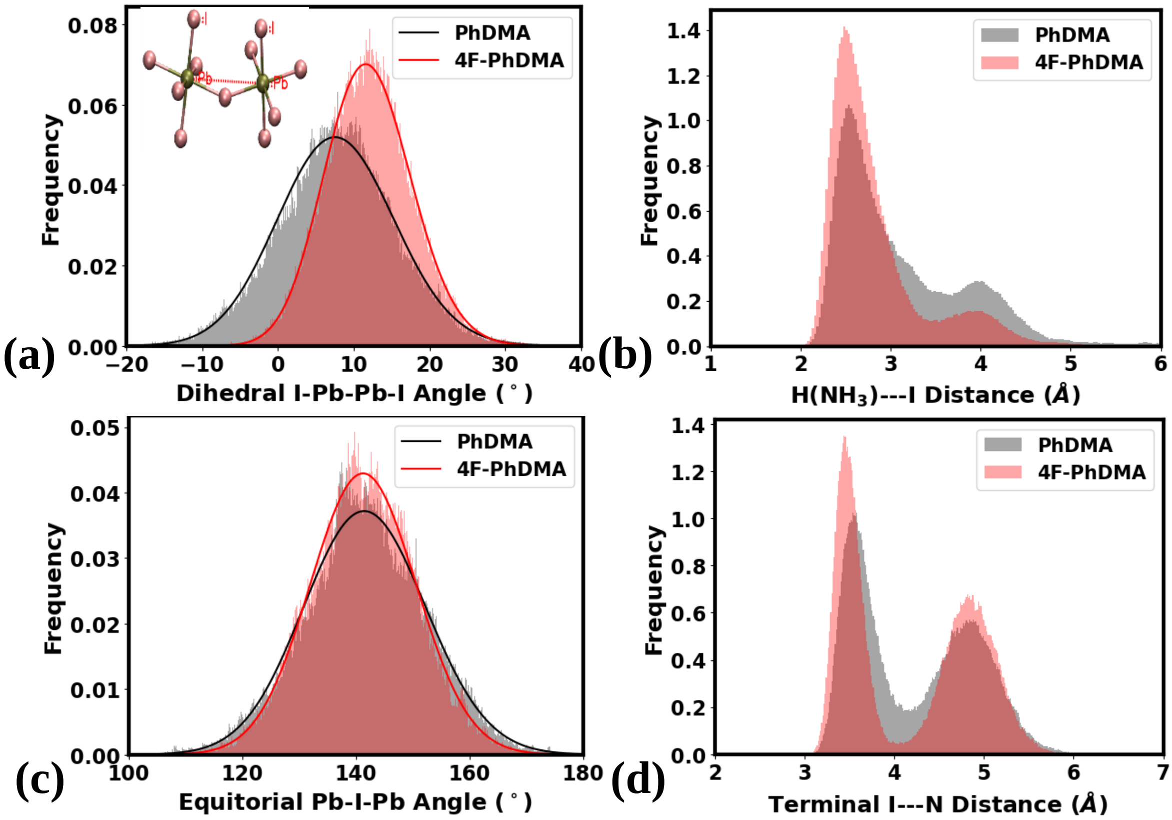

Figure S7: The histogram distribution plot of dynamic (a) axial dihedral I-Pb-Pb-I angle between two neighboring PbI$_6$ octahedra (b) distance between H of NH$_3$ head of organic spacer and I of PbI$_6$ octahedra (c) equatorial Pb-I-Pb bond angle of inorganic PbI$_6$ octahedra (d) distance between terminal I of PbI$_6$ octahedra and N of NH$_3$ head of organic spacer. The much narrower distribution of dihedral angles depicts that the in-plane octahedral tilting motions are considerably suppressed The Pb-I-Pb equatorial angle distributions are further plotted as a histogram to find the in-plane octahedral distortions. With fluorination in spacer cations, the angle distribution becomes moderately narrow as shown in (c).

Section S2. The Dynamic Structure of (PhDMA)PbI$_4$ and (4F-PhDMA)PbI$_4$

The structural dynamic and NCI plot analysis clarify favorable interactions between the fluorine of the spacer cation and the inorganic layer, lowering the thermal fluctuations. We know one spacer cation is placed between four PbI$_6$ octahedra above and four octahedra below. One fluorine or hydrogen of the aromatic ring simultaneously interacts with the two nearest terminal iodine of PbI$_6$ octahedra. In (4F-PhDMA)PbI$_4$, the fluorine of the aromatic ring is placed at an equidistance from the nearest two terminal iodine, unlike hydrogen of the aromatic ring of PhDMA. For a more detailed study, the dynamic interactions of aromatic H and F of both spacers with terminal iodine of the inorganic layer have been plotted for analysis. In the histogram plot (Figure 3d), the narrow distribution for (4F-PhDMA)PbI$_4$ indicates a consistent non-covalent interaction between F of the aromatic ring and terminal I of the inorganic layer. And this is because of the relatively symmetric arrangement of 4F-PhDMA spacer cation, as discussed in the NCI section. On the other hand, the distribution for non-covalent interaction between H of the aromatic ring and terminal I is spread over an extended range of bond distance. This indicates a very fluctuating and weak non-covalent interaction between the aromatic hydrogen of the spacer cation and terminal I of the inorganic layer. Furthermore, the ensemble average of Ph-F···I (terminal) is shorter for 4F-PhDMA as compared to Ph-H···I (terminal) distance. At a qualitative level, considering the dominating van-der-Waals interaction of Ph-F with terminal I, we can conclude that stronger non-covalent interactions between spacer cation and the inorganic layer, indeed, partially restrict the thermal motions of inorganic PbI_6 octahedra.

Furthermore, the distribution for N_{NH3}···I (terminal) distance (Figure S6(d)) shows the distance of the dynamic between N of NH_3 head of organic spacer and terminal iodine of inorganic PbI layer. The narrow distribution peak with a lower ensemble average for 4F-PhDMA indicates stronger and closer halogen-halogen interaction with reduced thermal fluctuation, unlike the PhDMA counterpart. The restricted dynamics of 4F-PhDMA result in more consistent van-der-Waals interactions.

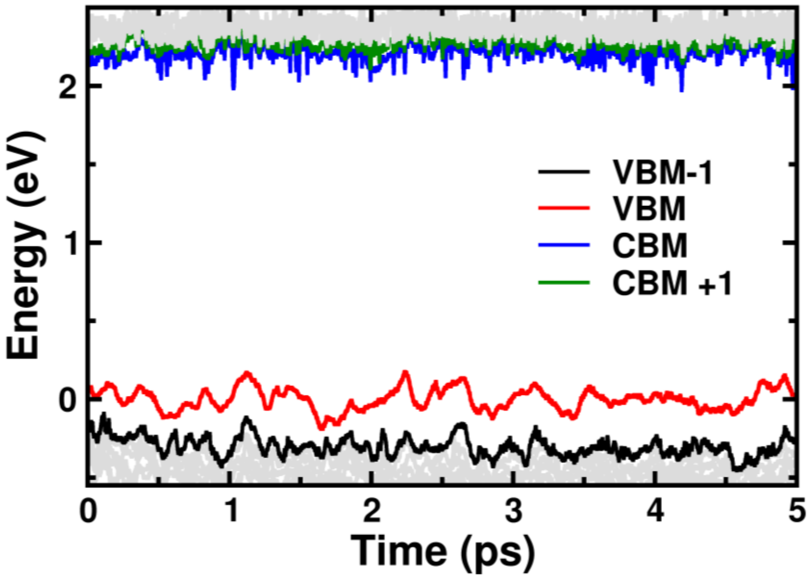

Figure S8. The energy states as a function of time in (4F-PhDMA)PbI_4. The VBM state remains well separated from other lower-lying valence band states. The fluctuations in the VBM and CBM energy states give rise to the distribution in band gap values over time.

Table S3. The time-averaged non-adiabatic coupling (NAC) strength for pairs of energy states in VB and CB of A′PbI_4. The tabulated pairs actively participate in the non-radiative recombination process of photogenerated charge carriers.

Energy states involved	NAC in (PhDMA)PbI_4 - (meV)	NAC in (4F-PhDMA)PbI_4 (meV)
(VBM-1) - VBM	7.3	-
(VBM-1) - CBM	0.24	-
(VBM-1) – (CBM+1)	0.24	-
(VBM) - CBM	0.35	0.39
(VBM) – (CBM+1)	0.37	0.45

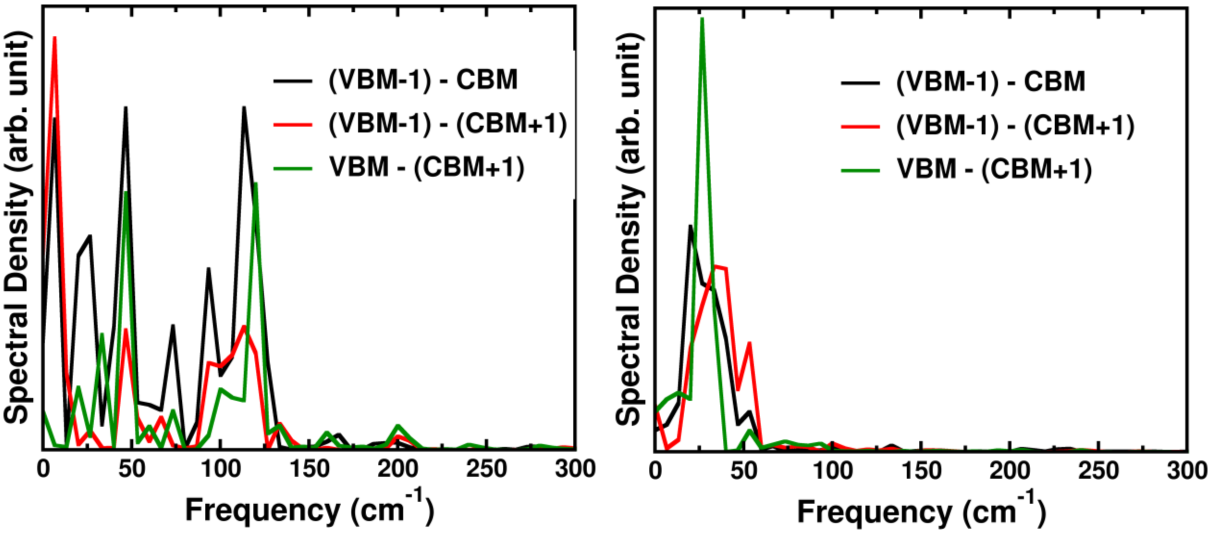

(a) (b)

Figure S9. The Fourier transform of autocorrelation for the energy gap fluctuations between two energy states in (a) (PhDMA)PbI_4 and (b) (4F-PhDMA)PbI_4. All the involved energy state pairs exhibit a broader range of frequencies for (PhDMA)PbI_4. This indicates a greater number of active phonon modes in (PhDMA)PbI_4 that couple with electronic states and contribute to the non-adiabatic charge carrier dynamics processes at 300 K. The y-axis scale is arbitrary but in consistent units.